PHYSICAL PROPERTIES OF NOVEL α-Fe₂O₃/NiO HETEROSTRUCTURES THROUGH IMMERSION/ SOL–GEL SPIN COATING METHOD: DIFFERENT DEPOSITION NUMBERS OF NiO LAYER

N. Parimon[a,b], M. H. Mamat[a,c*], A. B. Suriani[d], A. Mohamed[d], M. K. Ahmad[e], I. B. Shameem Banu[f], N. Vasimalai[f], M. Rusop[a,c]

[a]NANO-ElecTronic Centre (NET), School of Electrical Engineering, College of Engineering, Universiti Teknologi MARA, 40450 Shah Alam, Selangor, Malaysia
[b]Faculty of Engineering, Universiti Malaysia Sabah, 88400 Kota Kinabalu, Sabah, Malaysia
[c]NANO-SciTech Lab (NST), Center for Functional Materials and Nanotechnology, Institute of Science (IOS), Universiti Teknologi MARA, 40450 Shah Alam, Selangor, Malaysia
[d]Nanotechnology Research Centre, Faculty of Science and Mathematics, Universiti Pendidikan Sultan Idris (UPSI), 35900 Tanjung Malim, Perak, Malaysia
[e]Microelectronic and Nanotechnology–Shamsuddin Research Centre (MiNT-SRC), Faculty of Electrical and Electronic Engineering, Universiti Tun Hussein Onn Malaysia (UTHM), 86400 Batu Pahat, Johor, Malaysia
[f]School of Physical and Chemical Sciences, B.S. Abdur Rahman Crescent Institute of Science & Technology, Vandalur, Chennai 600 048, India

Graphical abstract
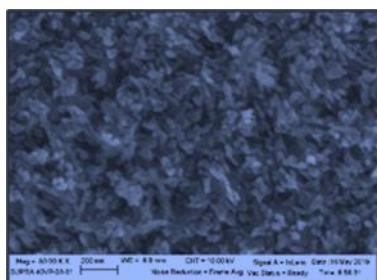
Abstract

The novel hematite (α-Fe₂O₃)/nickel oxide (NiO) heterostructures were grown on fluorine-doped tin oxide (FTO) coated glass substrates at various deposited NiO of 3, 5, and 7 layers. The heterostructures were successfully synthesized using the immersion and sol–gel spin coating methods for α-Fe₂O₃ and NiO films, respectively. The field emission scanning electron microscopy analysis showed that each sample of α-Fe₂O₃/NiO heterostructures has a unique surface morphology when deposited with different NiO layers. The X-ray diffraction pattern shows that the number of NiO layers affected the diffraction peaks. The NiO diffraction peak intensity at (111) plane increased when the deposition number of NiO layer was increased. The crystallite sizes of NiO were 35.4, 33.6, and 38.0 nm for 3-, 5-, and 7-layer NiO, respectively. The interplanar spacing, lattice parameter, and unit cell volume indicate NiO with 3-layer as the highest, while 5- and 7-layer had the same values. Meanwhile, the strain and stress values show the compressive strain and tensile stress, respectively. The optical properties reveal that the highest transmittance and the lowest absorbance percentages were recorded for a 3-layer NiO sample. In contrast, the lowest transmittance and the highest absorbance percentages were obtained for the sample with 5-layer NiO. Different thicknesses and morphologies of heterostructures explained these situations. In addition, each unique heterostructure of α-Fe₂O₃/NiO with high visible light absorption nature is perceived to reduce the bandgap energy and has the potential to be used in sensor and solar cell applications.

Keywords: α-Fe₂O₃/NiO heterostructure, immersion, sol–gel spin coating, sensor, solar cell
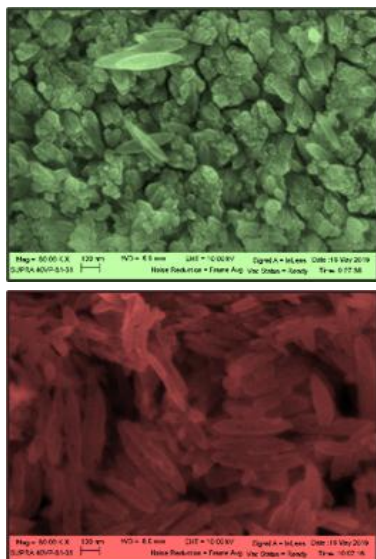
Abstrak

Heterostruktur hematit novel (α-Fe$_2$O$_3$)/nikel oksida (NiO) dihasilkan pada substrat kaca bersalut timah oksida terdop florin (FTO) dengan variasi pemendapan NiO dalam 3, 5, dan 7 lapisan. Heterostruktur ini berjaya disintesis masing-masing menggunakan kaedah perendaman dan lapisan putaran sol–gel bagi filem α-Fe$_2$O$_3$ dan NiO. Analisis mikroskopi elektron pengimbasan pelepasan medan menunjukkan bahawa setiap sampel heterostruktur α-Fe$_2$O$_3$/NiO mempunyai morfologi permukaan yang unik ketika dideposit dengan lapisan NiO yang berbeza. Corak difraksi sinar-X menunjukkan bilangan lapisan NiO mempengaruhi puncak difraksi. Keamatan puncak difraksi NiO pada satah (111) meningkat apabila bilangan pemendapan lapisan NiO ditingkatkan. Saiz kristal NiO didapati masing-masing ialah 35.4, 33.6, dan 38.0 nm untuk 3, 5, dan 7 lapisan NiO. Jarak antara planar, parameter kekisi, dan isipadu sel unit menunjukkan NiO dengan 3 lapisan adalah yang tertinggi, manakala NiO dengan 5 dan 7 lapisan menunjukkan nilai yang sama. Sementara itu, nilai terikan dan tegasan masing-masing menunjukkan terikan mampatan dan tegasan tegangan. Sifat optik menunjukkan bahawa peratusan transmisi tertinggi dan serapan terendah dicatatkan untuk sampel 3 lapisan NiO. Manakala, peratusan transmisi terendah dan serapan tertinggi diperoleh untuk sampel dengan 5 lapisan NiO. Ketebalan dan morfologi heterostruktur yang berbeza menjelaskan keadaan ini. Sebagai tambahan, setiap heterostruktur unik α-Fe$_2$O$_3$/NiO dengan sifat penyerapan cahaya yang tinggi dilihat dapat mengurangkan tenaga jurang dan berpotensi untuk digunakan dalam aplikasi sensor dan sel suria.

Kata kunci: heterostruktur α-Fe$_2$O$_3$/NiO, perendaman, lapisan putaran sol–gel, sensor, sel suria

1.0 INTRODUCTION

The use of mixed metal oxides has been rapidly increasing in various research areas due to their unique, distinctive, and tunable properties. Some mixed metal oxides perform well in their catalytic activity due to the changes in the surface area and electronic property [1-3]. The combination of at least two metal oxides in one network can revolutionize new chemical, physical, optical, and electrical properties resulting in higher performance of new technology [4, 5]. In addition, existing research also focus on the preparation of materials with small size and good stability, which can improve electrical characteristics of the materials particularly for device applications [6, 7]. With various approaches, a variety of heterostructured combinations based on metal oxides has been successfully produced. Ismail *et al.* fabricated SnO$_2$/ZnO heterojunction films for humidity sensors via a solution-based method [8]. Besides, Uddin *et al.* synthesized RuO$_2$/TiO$_2$ heterojunction nanocomposite for the photodecomposition of organic dyes and hydrogen production by methanol photoreforming [9]. Zhao *et al.* constructed the heterojunction of TiO$_2$–NiO using the hydrothermal method for efficient hydrogen generation and lignin photoreforming [10]. Pastrana *et al.* fabricated a-Fe$_2$O$_3$/CuO heterostructure-based thin film via a dip-coating approach for improved photoelectrochemical performance [11].

Generally, the studies on combining n-type hematite (α-Fe$_2$O$_3$) and p-type nickel oxide (NiO) have been reported using various strategies. The development of composites in constructing the heterostructures is useful in many applications, including gas sensors. For instance, Sun *et al.* synthesized Fe$_2$O$_3$-NiO heterostructure using a facile solvothermal process for the H$_2$S gas sensor [12]. Dong *et al.* prepared Fe$_2$O$_3$/NiO composites using the electrospinning and solution-phase reaction for ethanol gas sensing [13]. Besides, Tan *et al.* synthesized Fe$_2$O$_3$-loaded NiO heterojunction using microwave-assisted liquid-phase for responses to ethanol and methanol [14]. Nevertheless, there are other applications such as lithium-storage made from Fe$_2$O$_3$/NiO nanocomposites via cyanometallic framework-templated strategy by Chen *et al.* [15]. In addition, Zhang *et al.* developed Fe$_2$O$_3$/NiO heterostructure via in situ hydrothermal and cathodic electrodeposition processes for solar–chemical energy conversion in fuel cell [16]. All of these applications have proven that Fe$_2$O$_3$/NiO heterostructures can be widely used in various fields.

Among the available metal oxides, α-Fe$_2$O$_3$ and NiO are two multifunctional materials that have been extensively investigated for various applications, including dye-sensitized solar cells, electrochemical capacitors, catalysis, and lithium-ion batteries [13]. α-Fe$_2$O$_3$ is also known as iron oxide and it has a rhombohedral centered hexagonal structure [17]. It has a lower bandgap, E_g (2.1 eV), and is said to be the most stable iron oxide at ambient conditions [18]. Moreover, α-Fe$_2$O$_3$ is abundant, nontoxic, low cost, and suitable for use in sensors, catalysts pigments, and anode materials [17, 18]. Besides α-Fe$_2$O$_3$, NiO exhibits a broader bandgap, usually reported within 3.6–4.0 eV at room temperature [19, 20]. In addition to being considered transparent in the visible light region [21], NiO also possesses good electrical conductivity and a high surface to volume ratio [22].

There are various synthesis techniques in producing α-Fe_2O_3 nanostructures, such as precipitation [23], electrodeposition [24], and immersion [25]. The same goes for NiO nanostructures, which can be produced from various techniques, including radio frequency magnetron sputtering [26], immersion [27, 28], and sol–gel spin coating [29].

To the best of our knowledge, there are no reports of α-Fe_2O_3/NiO heterostructure studies with a combination of the immersion and sol–gel spin coating techniques. The immersion method is believed to be simpler and concise than the hydrothermal method because it does not require complex and time-consuming techniques. Meanwhile, the so-gel spin coating method is an appropriate approach for a thin film-forming in a controlled composition and nanostructure desired. Thus, in the present study, the α-Fe_2O_3 nanostructures were grown on fluorine-doped tin oxide (FTO) coated glass substrates using the immersion method. The FTO is one of the transparent conductive oxides chosen because it has a conductive layer and cheaper than the indium tin oxide (ITO) [30]. Further, different deposition numbers of NiO layer were deposited onto the α-Fe_2O_3 surface using the sol–gel spin coating technique. The effects of NiO layer variation on α-Fe_2O_3 to its morphological structure, crystalline phase, and optical properties were then examined for use in appropriate nanodevices.

2.0 METHODOLOGY

The FTO glass substrates were cleaned with ethyl alcohol as the first step before preparing the α-Fe_2O_3 layer. The solution of α-Fe_2O_3 is composed of a mixture of iron(III) chloride hexahydrate ($FeCl_3 \cdot 6H_2O$), urea (NH_2CONH_2), and deionized (DI) water, which was sonicated using an ultrasonic bath for 30 min at 50 °C. The solution was stirred using a hot plate magnetic stirrer for 5 min at 250 rpm. The solution was then poured into Schott bottles, where the FTO glass substrates were placed inside with the conductive FTO coatings facing up. The Schott bottles filled with the solutions were immersed in a water bath (Memmert) for 3 h at 95 °C. Then, the FTO coated glass substrates with α-Fe_2O_3 nanostructures were dried in a furnace for 10 min at 150 °C and annealed for 1 h at 500 °C.

For the deposition of different NiO layers on the surface of α-Fe_2O_3, the sol–gel spin coating technique was used. The solution of NiO involved a mixture of nickel(II) nitrate hexahydrate ($Ni(NO_3)_2 \cdot 6H_2O$), hexamethylenetetramine ($C_6H_{12}N_4$), and DI water. The solution was sonicated for 30 min and stirred in ambient for 45 min at 300 rpm. Twenty drops of the solution using a pipette dropper were used in the spin coating technique for each NiO layer on the α-Fe_2O_3 surface. The process was repeated with different NiO layers, which are 3, 5, and 7. Before the annealing process at 500 °C for 1 h

for the last layer, each of the completed α-Fe_2O_3/NiO heterostructure at the different numbers of NiO layer was dried at 250 °C for 5 min per layer. The heterostructure schematic, which was grown on the FTO coated glass substrate, is shown in Figure 1.
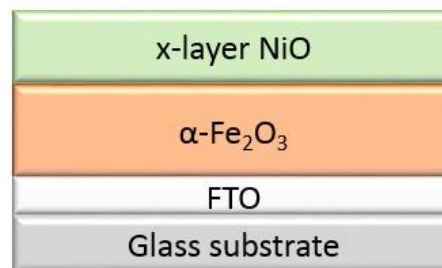

Figure 1 A schematic of the α-Fe_2O_3/NiO heterostructure (x = 3, 5, and 7)

The physical properties of α-Fe_2O_3/NiO heterostructures were analyzed for their surface morphological, structural, and optical properties. The surface morphological images were observed using field emission scanning electron microscopy (FESEM) (Zeiss Supra 40VP). The crystal structures were analyzed using X-ray diffraction (XRD) (PANalytical X'Pert PRO). The optical properties were characterized using the ultraviolet–visible–near infrared (UV–vis–NIR) spectrophotometer (Jasco-Lambda 750).

3.0 RESULTS AND DISCUSSION

3.1 Surface Morphology Observation

The FESEM images in Figure 2 show the surface morphologies of α-Fe_2O_3/NiO heterostructures with varied deposition numbers of NiO in (a) 3, (b) 5, and (c) 7 layers. The insets show a magnified view with the respective number of NiO layers. Each heterostructure was successfully grown uniformly, dense, and the most important is that each morphology is unique. The diffusion of NiO elements for different layers into α-Fe_2O_3 could be the reason for their changes in the morphologies.

As shown in Figure 2 (a), the surface morphology of α-Fe_2O_3/NiO at 3-layer NiO exhibits low surface roughness, small grain size, and delicate nanostructures. Meanwhile, the α-Fe_2O_3/NiO at 5-layer NiO in Figure 2 (b) shows a rougher and larger grain size. The inset image in Figure 2 (b) shows that the morphology is compact and some of the structures are close to the image in Figure 2 (c). Figure 2 (c) shows α-Fe_2O_3/NiO at 7-layer NiO with a different morphology. The morphology can be described in a fine nanorice-like structure (see the inset in Figure 2 [c]). The structure with more porous is quite similar to the hematite nanotubes obtained by

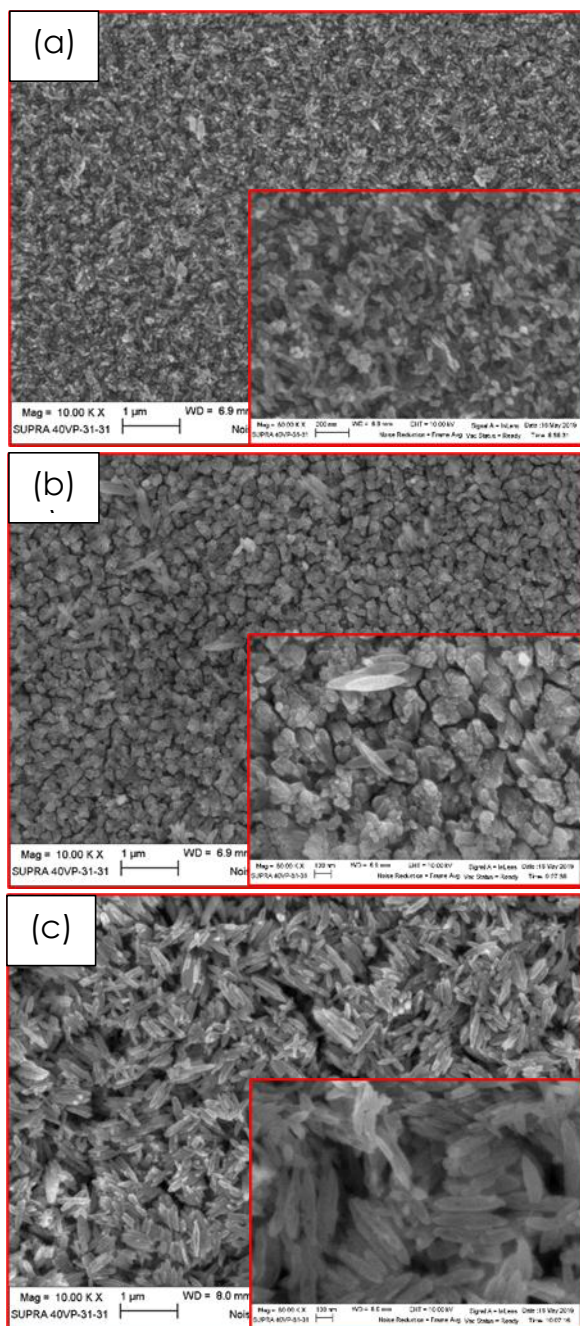Huo *et al.*, who used a hydrothermal approach [13], a solution-based method.

Figure 2 Surface morphologies of α -Fe$_2$O$_3$/NiO heterostructures with inset of magnified views at different deposition numbers of NiO layer: (a) 3, (b) 5, and 7 layers

3.2 X-Ray Diffraction Analysis

Figure 3 records the diffraction peaks of the formation α -Fe$_2$O$_3$/NiO heterostructures, which were synthesized on the FTO glass substrates. The observed peaks for the α -Fe$_2$O$_3$ are associated with the standard rhombohedral hexagonal phase indexed to JCPDS No. 33-0664 [25]. The diffraction peaks of α -

Fe$_2$O$_3$ are most observed when using 3-layer NiO at 24.4°, 33.4°, 36.0°, 41.0°, 49.7°, 54.4°, 62.7°, and 64.2°, which were indexed to (012), (104), (110), (113), (024), (116), (214), and (300) crystal planes, respectively. The number of peaks can be seen to decrease with the increasing NiO layers. Meanwhile, the diffraction peaks at 26.8°, 34.0°, 51.9°, 62.0°, 66.2°, and 81.2° corresponding to the FTO conductive layer were also recorded in the XRD patterns. Other peaks with high intensity can also be seen to match the polycrystalline NiO structure, which can be indexed to cubic β-NiO (JCPDS No. 47-1049). The sharpness of the peak can be seen at (111) crystal plane, where the intensity increases as the number of NiO layer is increased. This observation indicates that the degree of good NiO crystallization can be improved by increasing the NiO layer. Besides, it can be seen that the diffraction peaks of 5- and 7-layer a bit shifted towards higher diffraction angle compared to the 3-layer diffraction peak. To further investigate the XRD patterns of α -Fe$_2$O$_3$/NiO heterostructures, the crystal parameters of the NiO at (111) plane were calculated. The crystallite size (*D*) of NiO can be calculated using the Scherrer expression (1):

$$D = \frac{k\lambda}{\beta \cos \theta} \tag{1}$$

where *k* is a constant (0.94), λ is the X-rays wavelength (1.542 Å), β is the full width at half-maximum (fwhm), and θ is the angle of diffraction. From the expression, the widest fwhm will cause the smallest *D*, while the narrowest fwhm shows otherwise. The results shown in Table 1 reveal that the 7-layer NiO has the largest *D* (38 nm), and the 5-layer NiO has the smallest *D* (33.6 nm). As reported by Parimon *et al.*, during the crystal growth process, recrystallization and aggregation occur, which causes the variation in crystallite size [31]. Moreover, the crystallite size is strongly influenced by dislocation density (*δ*). From the recorded values in Table 1, the crystallite size is inversely proportional to the *δ* through the relation:

$$\delta = \frac{1}{D^2} \tag{2}$$

This statement is in line with the explanation by Zeid *et al.*, where the *D* decreases as the *δ* increases [32]. Meanwhile, the 3-layer NiO exhibits the highest interplanar spacing (*d*), lattice parameter (*a*), and unit cell volume (*V*). In contrast, the 5- and 7-layer NiO show the same values for the same parameters. The *d*, *a*, and *V* values were calculated using the following formulas:

$$d = \frac{n\lambda}{2 \sin \theta} \tag{3}$$

$$\frac{1}{d^2} = \frac{h^2 + k^2 + l^2}{a^2} \tag{4}$$

$$V = a^3 \tag{5}$$

where n is the order value of diffraction (1), and h, k, and l are the Miller indices of the plane. Meanwhile, the strain (ε) and stress (σ) values show the compressive strain (negative value) and tensile stress (positive value), respectively. The following equations calculate were used to obtain the strain and stress values, respectively:

$$\varepsilon = \frac{a - a_o}{a_o} \times 100 \tag{6}$$

$$\sigma = \frac{E(a - a_o)}{2a_o p} \tag{7}$$

where a_o = 4.1771 Å is the lattice constant of the bulk NiO, E is the Young's modulus (200 GPa), and p is the Poisson ratio (0.31). Table 1 summarizes all the crystal parameters.
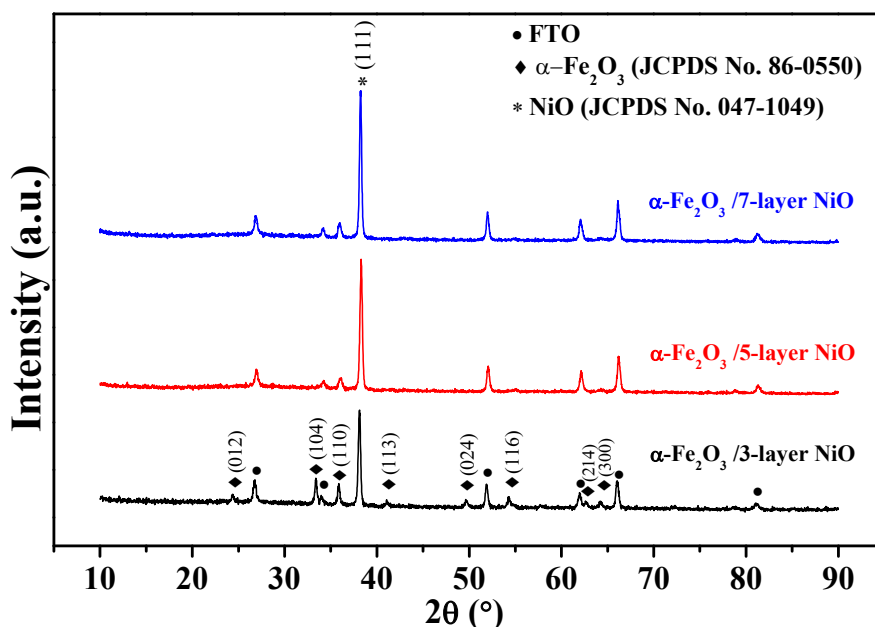

Figure 3 X-ray diffraction patterns of α-Fe$_2$O$_3$/NiO heterostructures at different deposition numbers of NiO layer

Table 1 The crystal parameters of the NiO at (111) plane

Sample (α-Fe$_2$O$_3$/x-layer NiO)	2θ (°)	Full width at half-maximum (fwhm), β (°)	Interplanar spacing, d (Å)	Lattice parameter, a (Å)	Unit cell volume, V $\times 10^{-29}$ (m^3)	Strain, ε (%)	Stress, σ (GPa)	Dislocation density, δ $\times 10^{14}$ (lines/m^2)	Crystallite size, D (nm)
x = 3	38.137	0.2484	2.3600	4.0876	6.83	−2.14	6.91	7.99	35.4
x = 5	38.261	0.2616	2.3526	4.0748	6.77	−2.45	7.90	8.86	33.6
x = 7	38.261	0.2315	2.3526	4.0748	6.77	−2.45	7.90	6.94	38.0

3.3 Transmittance and Absorbance

The optical properties of α-Fe$_2$O$_3$/NiO heterostructures were determined from the transmittance and absorbance spectra, as indicated in Figure 4 (a) and (b), respectively. The wavelength of the spectrum is in the UV–vis–NIR range from 300 to 1000 nm. As observed in Figure 4 (a), the highest transmittance percentage at 1000 nm for all samples show less than 50%, which are 49%, 12%, and 35% for 3-, 5-, and 7-layer NiO, respectively. The transmittance percentage values are almost static at approximately 0% in the UV region. The transmittances then increase slowly in the visible region. From 550 nm onwards, the transmittances

increase rapidly up to 1000 nm. Generally, low transmittances for all three α-Fe$_2$O$_3$/NiO heterostructures may be due to the thick layers that do not allow incident light to pass easily. The variations in transmittance value with different NiO layers prove that they produced varying thicknesses and various surface conditions. However, an increase in the deposition of the NiO layer does not necessarily indicate an increase in overall film thickness particularly when depositing on a rough and porous film of α-Fe2O3. From the transmittance spectra, the highest transmittance percentage by 3-layer NiO shows the lowest thickness, while the lowest transmittance percentage by 5-layer NiO shows otherwise. In other observation, the segregation

between particles happened on the sample with 7-layer NiO that caused the microscopic crack and uneven or non-uniform thickness. Therefore, this inter-particle segregation impacted the surface structure that caused the thickness to be lower than 5-layer NiO [33]. The segregation between particles happened due to stress evolution during the thermal heating and cooling process, which became obvious at 7-layer NiO. This condition is caused by the thermal coefficient difference between two or more materials. The stress in the films is highly dependent on annealing temperature, thickness, and chemical contents [34-36]. Besides, the different transmittances may be due to the various morphologies, shapes, defect states, and sizes as well as porous structures when varying the number of NiO layers on α-Fe$_2$O$_3$ structures [37]. As mentioned previously, 5-layer NiO has a compact and less porous structure than 7-layer NiO which causes its transmittance to be the lowest.

Figure 4 (b) shows the UV–vis–NIR absorption spectrum for α-Fe$_2$O$_3$/NiO heterostructures. The relation between transmittance (T) and absorbance (A) can be attributed by the following expression:

$$A = log_{10} \frac{1}{T} \qquad (8)$$

The absorbance percentage on the y-axis is the amount of light absorbed. The higher the percentage value, the more of a certain wavelength is absorbed. The spectra reveal that the lowest absorbance percentage belongs to the deposition with 3-layer NiO, where the absorption edge approached the shorter wavelength. It indicates that it has the largest energy bandgap as it requires more energy to jump. Meanwhile, the use of 5-layer NiO exhibited the highest absorbance percentage, and the absorption edges shifted to the longer wavelength. It shows that it has the smallest energy bandgap as it requires less energy to jump. As can be seen from the spectral ranges between 300 and 1000 nm, all the sample's absorption was observed more in the UV–vis region and hardly manifested an absorption in the NIR region. More precisely, the absorption edge is in the visible region. Considering that most of the visible light occupies the solar spectrum, these α-Fe$_2$O$_3$/NiO heterostructures can be exposed to maximize the use of sunlight [11, 16]. From the absorption spectrum, it can be perceived that the range of optical bandgap is estimated between 1.60 and 1.9 eV, which is the highest optical bandgap when 3-layer NiO was used, while the lowest bandgap was achieved when 5-layer NiO was used. It shows that the combination of heterostructures between α-Fe$_2$O$_3$ and NiO reduced the bandgap than the single α-Fe$_2$O$_3$ by enhancing the visible light absorption.
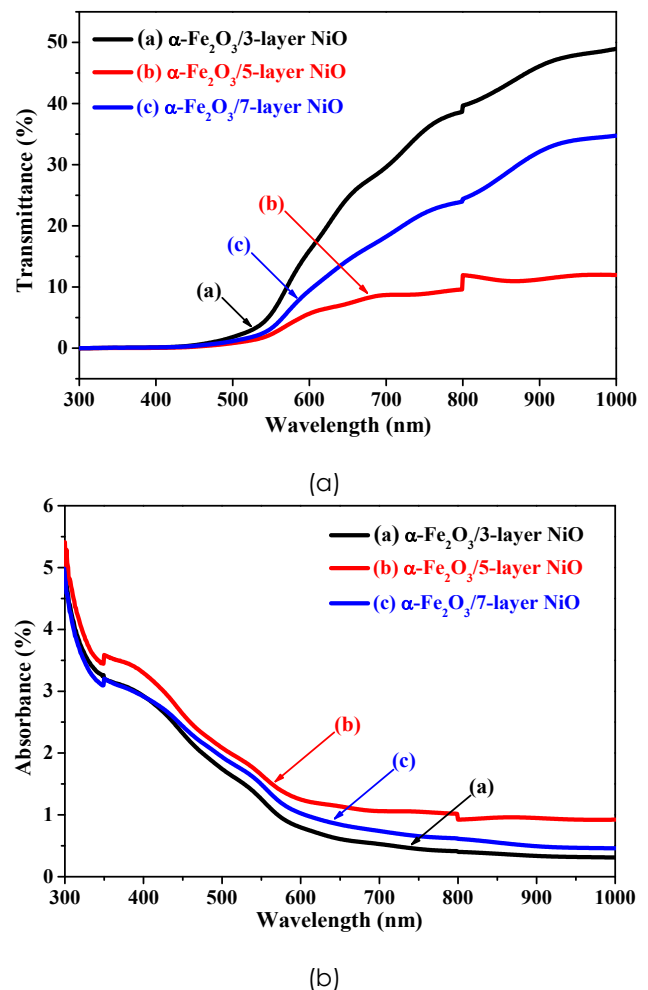

(a)

(b)

Figure 4 (a) Transmittance and (b) absorbance spectra of α-Fe$_2$O$_3$/NiO heterostructures at different deposition numbers of NiO layer

4.0 CONCLUSION

At the first stage of heterostructures formation, α-Fe$_2$O$_3$ layers were successfully grown on the FTO coated glass substrates using the immersion method. Various NiO layers were then deposited on the α-Fe$_2$O$_3$ utilizing the spin coating method. We have studied the effects of different NiO layers toward their morphological, structural, and optical properties. From the FESEM observation, the unique morphologies of α-Fe$_2$O$_3$/NiO heterostructures changed from 3- to 7-layer NiO. The XRD patterns show that there is only one peak of NiO corresponding to the (111) plane observed for all the samples. It can be observed that the higher the deposition number of the NiO layer, the higher the intensity of the NiO peak resulting in a good crystallinity. However, the crystallite size (D) did not follow the trend with the increase in the NiO layers because it was influenced by the dislocation density (δ). The D values were 35.4, 33.6, and 38.0 nm for 3-, 5-, and 7-layer NiO, respectively. The highest interplanar spacing (d), lattice parameter (a), and

unit cell volume (*V*) were obtained for 3-layer NiO, while 5- and 7-layer NiO showed the same values for the same parameters. The strain (*ε*) and stress (*σ*) values reveal the compressive strain and tensile stress, respectively. The deposition number of NiO layers also influenced the optical properties of α-Fe$_2$O$_3$/NiO heterostructures. The transmittances show that the variation of NiO layers resulted in percentages below 50%. Optical bandgap estimation from the absorbance spectra indicates that α-Fe$_2$O$_3$/NiO heterostructures with enhanced visible light absorption have a significant indicator in future sensor and solar cell applications.

Acknowledgment

References

[1] M. B. Gawande, R. K. Pandey, and R. V. Jayaram. 2012. Role of Mixed Metal Oxides in Catalysis Science—Versatile Applications in Organic Synthesis. *Catalysis Science & Technology*. 2(6): 1113-1125.
DOI: https://doi.org/10.1039/c2cy00490a.

[2] M. M. Yusoff, M. H. Mamat, M. A. R. Abdullah, A. S. Ismail, M. F. Malek, A. S. Zoolfakar, S. A. M. Al Junid, A. B. Suriani, A. Mohamed, M. K. Ahmad, I. B. Shameem Banu, and M. Rusop. 2020. Coupling Heterostructure of Thickness-Controlled Nickel Oxide Nanosheets Layer and Titanium Dioxide Nanorod Arrays Via Immersion Route for Self-powered Solid-state Ultraviolet Photosensor Applications. *Measurement*. 149: 106982.
DOI: https://doi.org/10.1016/j.measurement.2019.106982.

[3] N. D. Md Sin, M. H. Mamat, M. F. Malek, and M. Rusop. 2014. Fabrication of Nanocubic ZnO/SnO2 Film-based Humidity Sensor with High Sensitivity by Ultrasonic-assisted Solution Growth Method at Different Zn:Sn Precursor Ratios. *Applied Nanoscience*. 4 (7): 829-838
DOI: https://doi.org/10.1007/s13204-013-0262-5.

[4] M. Rashad, A. A. A. Darwish, and S. E. AlGarni. 2019. High Electrical Conductivity of (1-x)NiO/xFe2O3(x = 0.0, 0.3, 0.5, 0.7 and 1) Nanoparticles for Solid state Electronics. *Journal of Magnetism and Magnetic Materials*. 491: 165577.
DOI: https://doi.org/10.1016/j.jmmm.2019.165577.

[5] A. S. Ismail, M. H. Mamat, M. M. Yusoff, M. F. Malek, A. S. Zoolfakar, R. A. Rani, A. B. Suriani, A. Mohamed, M. K. Ahmad, and M. Rusop. 2018. Enhanced Humidity Sensing Performance using Sn-Doped ZnO Nanorod Array/SnO2 Nanowire Heteronetwork Fabricated Via Two-step Solution Immersion. *Materials Letters*. 210: 258-262.
DOI: https://doi.org/10.1016/j.matlet.2017.09.040.

[6] A. Mohamed, T. Ardyani, S. Abu Bakar, M. Sagisaka, Y. Umetsu, J. J. Hamon, B. A. Rahim, S. R. Esa, H. P. S. Abdul Khalil, M. H. Mamat, S. King, and J. Eastoe. 2018. Rational Design of Aromatic Surfactants for Graphene/Natural Rubber Latex Nanocomposites with Enhanced Electrical Conductivity. *Journal of Colloid and Interface Science*. 516: 34-47.
DOI: https://doi.org/10.1016/j.jcis.2018.01.041.

[7] M. H. Mamat, N. N. Hafizah, and M. Rusop. 2013. Fabrication of Thin, Dense and Small-diameter Zinc Oxide Nanorod Array-based Ultraviolet Photoconductive Sensors with High Sensitivity by Catalyst-free Radio Frequency Magnetron Sputtering. *Materials Letters*. 93: 215-218.
DOI: https://doi.org/10.1016/j.matlet.2012.11.105.

[8] A. S. Ismail, M. H. Mamat, M. F. Malek, M. M. Yusoff, R. Mohamed, N. D. M. Sin, A. B. Suriani, and M. Rusop. 2018. Heterogeneous SnO2/ZnO Nanoparticulate Film: Facile Synthesis and Humidity Sensing Capability. *Materials Science in Semiconductor Processing*. 81: 127-138.
DOI: https://doi.org/10.1016/j.mssp.2018.03.022.

[9] M. T. Uddin, O. Babot, L. Thomas, C. Olivier, M. Redaelli, M. D'Arienzo, F. Morazzoni, W. Jaegermann, N. Rockstroh, H. Junge, and T. Toupance. 2015. New Insights into the Photocatalytic Properties of RuO2/TiO2Mesoporous Heterostructures for Hydrogen Production and Organic Pollutant Photodecomposition. *The Journal of Physical Chemistry C*. 119(13): 7006-7015.
DOI: https://doi.org/10.1021/jp512769u.

[10] H. Zhao, C.-F. Li, L.-Y. Liu, B. Palma, Z.-Y. Hu, S. Renneckar, S. Larter, Y. Li, M. G. Kibria, J. Hu, and B.-L. Su. 2020. n-p Heterojunction of TiO2-NiO Core-shell Structure for Efficient Hydrogen Generation and Lignin Photoreforming. *Journal of Colloid and Interface Science*. 585: 694-704.
DOI: https://doi.org/10.1016/j.jcis.2020.10.049.

[11] E. C. Pastrana, V. Zamora, D. Wang, and H. Alarcón. 2019. Fabrication and Characterization of a-Fe2O3/CuO Heterostructure Thin Films via Dip-Coating Technique for Improved Photoelectrochemical Performance. *Advances in Natural Sciences: Nanoscience and Nanotechnology*. 10(3): 035012.
DOI: https://doi.org/10.1088/2043-6254/ab3d2f.

[12] G.-J. Sun, H. Kheel, J. K. Lee, S. Choi, S. Lee, and C. Lee. 2016. H2S Gas Sensing Properties of Fe2O3 Nanoparticle-Decorated NiO Nanoplate Sensors. *Surface and Coatings Technology*. 307: 1088-1095.
DOI: https://doi.org/10.1016/j.surfcoat.2016.06.066.

[13] S. Dong, D. Wu, W. Gao, H. Hao, G. Liu, and S. Yan. 2020. Multi-dimensional Templated Synthesis of Hierarchical Fe2O3/NiO Composites and Their Superior Ethanol Sensing Properties Promoted by Nanoscale p-n Heterojunctions. *Dalton Trans*. 49(4): 1300-1310.
DOI: https://doi.org/10.1039/C9DT04185K

[14] W. Tan, J. Tan, L. Fan, Z. Yu, J. Qian, and X. Huang. 2018. Fe2O3-loaded NiO Nanosheets for Fast Response/Recovery and High Response Gas Sensor. *Sensors and Actuators B: Chemical*. 256: 282-293.
DOI: https://doi.org/10.1016/j.snb.2017.09.187.

[15] Y. Chen, R. Cai, Y. Yang, C. Liu, A. Yuan, H. Yang, and X. Shen. 2017. Cyanometallic Frameworks Derived Hierarchical Porous Fe 2 O 3 /NiO Microflowers with Excellent Lithium-storage Property. *Journal of Alloys and Compounds*. 698: 469-475.
DOI: https://doi.org/10.1016/j.jallcom.2016.12.230.

[16] D. Zhang, Y. Wang, Y. Wang, Y. Zhang, and X.-M. Song. 2020. Fe2O3/NiO Photocathode for Photocatalytic Methanol Fuel Cell: An Insight on Solar Energy Conversion. *Journal of Alloys and Compounds*. 815: 152377.
DOI: https://doi.org/10.1016/j.jallcom.2019.152377.

[17] Caihua Wang, Yumin Cui, and K. Tang. 2013. One-pot Synthesis of a-Fe2O3 Nanospheres by Solvothermal Method. *Nanoscale Research Letters*. 8: 213-216.
DOI: https://doi.org/10.1186/1556-276X-8-213.

[18] Y. Huo, Y. Zhu, J. Xie, G. Cao, T. Zhu, X. Zhao, and S. Zhang. 2013. Controllable Synthesis of Hollow a-Fe2O3 Nanostructures, Their Growth Mechanism, and the Morphology-reserved Conversion to Magnetic Fe3O4/C Nanocomposites. *RSC Advances*. 3(41): 19097.
DOI: https://doi.org/10.1039/c3ra42764a.

[19] M. H. Mamat, N. Parimon, A. S. Ismail, I. B. Shameem Banu, S. Sathik Basha, G. V. Vijayaraghavan, M. K. Yaakob, A. B. Suriani, M. K. Ahmad, and M. Rusop. 2019. Structural, Optical, and Electrical Evolution of Sol–Gel-Immersion Grown Nickel Oxide Nanosheet Array Films on Aluminium

doping. *Journal of Materials Science: Materials in Electronics*. 30(10): 9916-9930.
DOI: https://doi.org/10.1007/s10854-019-01330-z.

[20] N. Parimon, M. H. Mamat, M. K. Ahmad, I. B. Shameem Banu, and M. Rusop. 2019. Highly Porous NiO Nanoflower-based Humidity Sensor Grown on Seedless Glass Substrate via One-Step Simplistic Immersion Method. *International Journal of Engineering and Advanced Technology*. 9(1): 5718-5722.
DOI: https://doi.org/10.35940/ijeat.A3052.109119.

[21] Z. H. Ibupoto, M. A. Abbasi, X. Liu, M. S. AlSalhi, and M. Willander. 2014. The Synthesis of NiO/TiO2Heterostructures and Their Valence Band Offset Determination. *Journal of Nanomaterials*. 2014: 1-6.
DOI: https://doi.org/10.1155/2014/928658.

[22] N. Parimon, M. H. Mamat, M. A. R. Abdullah, A. S. Ismail, W. R. W. Ahmad, I. B. S. Banu, and M. Rusop. 2018. Nanocarnation-like Nickel Oxide Thin Film: Structural and Optical Properties. *International Journal of Engineering & Technology*. 7(4): 103-106.

[23] N. Sankova and E. Parkhomchuk. 2020. Pseudomorphism and Size Stabilization of Hematite Particles in the Organic Phase Synthesis. *Journal of Solid State Chemistry*. 282: 121130.
DOI: https://doi.org/10.1016/j.jssc.2019.121130.

[24] L. Li, P. Liang, C. Liu, H. Zhang, N. Mitsuzaki, and Z. Chen. 2019 New Method for Improving the Bulk Charge Separation of Hematite with Enhanced Water Splitting. *International Journal of Hydrogen Energy*. 44(8): 4208-4217.
DOI: https://doi.org/10.1016/j.ijhydene.2018.12.125.

[25] W. R. W. Ahmad, M. H. Mamat, Z. Khusaimi, A. S. Ismail, and M. Rusop. 2019. Impact of Annealing Temperature to the Performance of Hematite-based Humidity Sensor. *Indonesian Journal of Electrical Engineering and Computer Science*. 13: 1079-1086.
DOI: https://doi.org/10.11591/ijeecs.v13.i3.pp1079-1086.

[26] H. Lee, Y. T. Huang, M. W. Horn, and S. P. Feng. 2018. Engineered Optical and Electrical Performance of Rf-Sputtered Undoped Nickel Oxide Thin Films for Inverted Perovskite Solar Cells. *Sci Rep*. 8(1): 5590.
DOI: https://doi.org/10.1038/s41598-018-23907-0.

[27] M. A. R. Abdullah, M. H. Mamat, A. S. Ismail, M. F. Malek, A. B. Suriani, M. K. Ahmad, I. B. Shameem Banu, R. Amiruddin, and M. Rusop. 2019. Direct and Seedless Growth of Nickel Oxide Nanosheet Architectures on ITO using a Novel Solution Immersion Method. *Materials Letters*. 236: 460-464.
DOI : https://doi.org/10.1016/j.matlet.2018.10.163.

[28] M. H. Mamat, N. Parimon, A. S. Ismail, I. B. S. Banu, S. Sathik Basha, R. A. Rani, A. S. Zoolfakar, M. F. Malek, Suriani, M. K. Ahmad, and M. Rusop. 2020. Synthesis, Structural and Optical Properties of Mesostructured, X-doped NiO (X = Zn, Sn, Fe) Nanoflake Network Films. *Materials Research Bulletin*. 127: 110860.
DOI: https://doi.org/10.1016/j.materresbull.2020.110860.

[29] N. F. Q. Fahmi, M. H. Mamat, A. S. Zoolfakar, A. H. A. Razak, and M. Rusop. 2019. Effect of Zn-Doping on the Structural, Optical, and Humidity Sensing Properties of Sol-Gel Synthesized NiO Thin Film. *International Journal of Recent Technology and Engineering*. 8(4): 6745-6749.
DOI: https://doi.org/10.35940/ijrte.D5216.118419.

[30] A. Way, J. Luke, A. D. Evans, Z. Li, J.-S. Kim, J. R. Durrant, H. K. Hin Lee, and W. C. Tsoi. 2019. Fluorine Doped Tin Oxide as an Alternative of Indium Tin Oxide for Bottom Electrode of Semi-transparent Organic Photovoltaic Devices. *AIP Advances*. 9(8): 085220.
DOI: https://doi.org/10.1063/1.5104333

[31] N. Parimon, M. H. Mamat, I. B. Shameem Banu, N. Vasimalai, M. K. Ahmad, A. B. Suriani, A. Mohamed, and M. Rusop. 2020. Fabrication, Structural, Optical, Electrical, and Humidity Sensing Characteristics of Hierarchical Nio Nanosheet/Nanoball-Flower-Like Structure Films. *Journal of Materials Science: Materials in Electronics*. 31(14): 11673-11687.
DOI: https://doi.org/10.1007/s10854-020-03719-7.

[32] E. F. A. Zeid, I. A. Ibrahem, A. M. Ali, and W. A. A. Mohamed. 2019. The Effect of CdO Content on the Crystal Structure, Surface Morphology, Optical Properties and Photocatalytic Efficiency of p-NiO/n-CdO Nanocomposite. *Results in Physics*. 12: 562-570.
DOI: https://doi.org/10.1016/j.rinp.2018.12.009.

[33] S. Swaminarayan and D. J. Srolovitz. 1996. Surface Segregation in Thin Films. *Acta Materialia*. 44(5): 2067-2072.
DOI: https://doi.org/10.1016/1359-6454(95)00282-0.

[34] M. Zainizan Sahdan, M. Hafiz Mamat, M. Salina, Z. Khusaimi, U. M. Noor, and M. Rusop. 2010. Heat Treatment Effects on the Surface Morphology and Optical Properties of ZnO Nanostructures. *Physica Status Solidi c*. 7(9): 2286-2289.
DOI: https://doi.org/10.1002/pssc.200983722.

[35] H. Kozuka. Stress Evolution and Cracking in Sol-Gel-Derived Thin Films. 2018. *Handbook of Sol-Gel Science and Technology: Processing, Characterization and Applications*, L. Klein, M. Aparicio, and A. Jitianu Eds. Cham: Springer International Publishing. 275-311.
DOI: https://doi.org/10.1007/978-3-319-32101-1_12.

[36] T. Sakorikar, M. K. Kavitha, P. Vayalamkuzhi, and M. Jaiswal. 2017. Thickness-dependent Crack Propagation in Uniaxially Strained Conducting Graphene Oxide Films on Flexible Substrates. *Scientific Reports*. 7(1): 2598.
DOI: 10.1038/s41598-017-02703-2.

[37] M. H. Mamat, M. F. Malek, N. N. Hafizah, M. N. Asiah, A. B. Suriani, A. Mohamed, N. Nafarizal, M. K. Ahmad, and M. Rusop. 2016. Effect of Oxygen Flow Rate on the Ultraviolet Sensing Properties of Zinc Oxide Nanocolumn Arrays Grown by Radio Frequency Magnetron Sputtering. *Ceramics International*. 42(3): 4107-4119.
DOI: https://doi.org/10.1016/j.ceramint.2015.11.083.